JOURNAL OF CHEMICAL PHYSICS VOLUME 115, NUMBER 16 22 OCTOBER 2001

Quadrupolar-shielding cross-correlations in solid state nuclear magnetic resonance: Detecting antisymmetric components in chemical shift tensors

Sungsool Wi and Lucio Frydman[a)]
Department of Chemical Physics, Weizmann Institute of Sciences, 76100 Rehovot, Israel, and Department of Chemistry, University of Illinois at Chicago, Chicago, Illinois 60607

(Received 22 June 2001; accepted 7 August 2001)

This work investigates the nature of second order effects resulting in solid state nuclear magnetic resonance (NMR), from cross-correlations between the quadrupolar and shielding couplings. Using an average Hamiltonian theory, it is shown that these effects can bring the nonsecular terms of the shielding interaction into the realm of conventional detection. Such terms include the antisymmetric components of the chemical shift tensor, which, although postulated to exist, have hitherto eluded direct experimental measurement. As numerical calculations supported these analytical derivations, an experimental study was undertaken to measure such components from the single-crystal rotation plot of a half-integer quadrupolar nucleus. A custom-made probehead was built, a data analysis procedure developed, and together these were used to analyze the satellite transition spectra arising from a ^{59}Co single crystal of cobalt(III)tris(acetylacetonate). The results of repetitive studies on such sample are reported. [DOI: 10.1063/1.1406533]

I. INTRODUCTION

The chemical shift counts among the most important observables available in nuclear magnetic resonance (NMR). This interaction reflects secondary fields induced at the nuclear sites when a molecule or lattice is inserted inside a strong external magnetic flux. Such fields depend on the local electronic environment surrounding a particular nucleus, and provide different resonant frequencies to chemically inequivalent sites. These electron-induced shifts also depend on the relative orientation of the molecular orbitals with respect to the main NMR magnetic field, a variation that can be described mathematically by a spatial tensor with rank $l \leqslant 2$. When expressed in terms of Cartesian components, each element of the resulting second-rank chemical shift $\{\delta_{ij}\}$ tensor can be decomposed as[1–3]

$$\delta_{ij}=\underset{\substack{l=0\\ \text{(isotropic)}}}{\frac{1}{3}\sum_{i=1}^{3}\delta_{ii}}+\underset{\substack{l=1\\ \text{first-rank}}}{\frac{[\delta_{ij}-\delta_{ji}]}{2}}+\underset{\substack{l=2\\ \text{(second-rank)}}}{\left[\frac{\delta_{ij}+\delta_{ji}}{2}-\frac{1}{3}\sum_{i=1}^{3}\delta_{ii}\right]}. \qquad (1)$$

Molecules in fluids execute rapid isotropic tumblings; only the orientation-independent $l=0$ component remains then observable, leading to the sharp high resolution spectra usual in solution or gas phase NMR. In solids, however, higher rank components may also remain unaveraged, including an $l=1$ antisymmetric chemical shift (ACS) contribution and an $l=2$ chemical shift anisotropy (CSA).

The actual Hamiltonian originating from the chemical shielding will be given by products of the spatial shielding components in Eq. (1), times $\{T_{l,-m}\}_{l=0-2,-l\leqslant m\leqslant l}$ terms containing the spin operators.[1–4] In the high-field regime where the Zeeman interaction $H_Z=\omega_0 T_{1,0}$ is dominant, only those products proportional to $T_{l,0}$ will remain secular. In Eq. (1) both $l=0$ and $l=2$ contributions contain such terms, and hence they appear as first order corrections to the Zeeman transition frequency. Their typical magnitudes are in the order of $\delta_{ij}\omega_0/2\pi\approx 10^0-10^4$ Hz, only a few ppms of the Larmor frequency yet easily measurable by conventional NMR standards. By contrast, ACS contributions only contain nonsecular $T_{1,\pm 1}$ spin terms.[1] Their Hamiltonian therefore appears as a second order effect of magnitude $(\delta_{ij})^2\cdot\omega_0/2\pi \leqslant 1$ Hz, small enough to have eluded so far the solid state NMR measurements that could detect them. This, however, does not imply that ACS terms are necessarily smaller than their secular shielding counterparts. In fact, theoretical calculations indicate that nuclei located at sites with low symmetry are characterized by ACS and CSA couplings of similar orders of magnitudes.[5,6] Furthermore, solution state NMR relaxation rates, in which both secular and nonsecular shielding terms appear equally weighted as second order effects, have been estimated to include in favorable cases up to 20% contributions from antisymmetric effects.[7]

Though generally harder to detect than their first order counterparts, the experimental NMR observation of nonsecular terms within a Hamiltonian H_λ is not unknown.[8–20] In a majority of instances this happens when quadrupolar nuclei are involved; a tilting in the axis of quantization brought about by the quadrupolar interaction Q then enables such terms to show up as second order cross correlations. Probably best-documented among these phenomena is the second order quadrupole effect ($H_\lambda=H_Q$), a dominating feature in the central transition spectroscopy of half-integer quadrupole nuclei.[8–10] Given Zeeman and quadrupole coupling frequencies ω_0,χ_Q, these effects end up proportional to χ_Q^2/ω_0,

---

[a)] Author to whom correspondence should be addressed: Lucio Frydman, Department of Chemical Physics, Weizmann Institute of Science, 76100 Rehovot, Israel, Fax: +972-8-9344123, Electronic mail: lucio.frydman@weizmann.ac.il often in the 10^3-10^5 Hz regime. Another manifestation of second order effects are the residual I-S splittings that can sometimes be observed, even under fast magic-angle-spinning (MAS), when dipolar couplings d_{IS} to quadrupolar $I\geqslant 1$ nuclei are involved.[11–15] In magnitude this effect is then proportional to $d_{IS}\cdot\chi_Q^1/\omega_0^1$. Yet another example of such quadrupole-enabled phenomena arises in overtone spectroscopy,[16–20] which involves $H_{\lambda'}=H_{rf}$ and gives origin to the excitation of otherwise forbidden multi-quantum transitions at nutation rates $\propto\omega_{rf}\cdot\chi_Q/\omega_0$.

When extended to the case of the chemical shielding interaction, these considerations predict that both ACS as well as other nonsecular shielding contributions might manifest themselves in the spectra of quadrupolar nuclei, as frequency shifts in the order of $(\delta_{ij}\omega_0)\cdot\omega_Q/\omega_0$. This represents magnitudes of ppms of the quadrupole coupling constant, and hence measurable under moderate-to-strong quadrupole and shielding coupling conditions. In fact these effects have apparently been recently noticed in a highly accurate MAS NMR investigation of ^{14}N, a spin-1 nucleus.[21] The present paper further discusses hitherto unexplored aspects of these quadrupolar-shielding cross-correlations in solid state NMR, focusing in particular on their potential application to the measurement of the antisymmetric chemical shift components. As basis for such analysis the following section introduces an analytical high-field form for the Hamiltonian that describes shielding-quadrupolar second order effects. The resulting expressions reveal that both ACS and CSA effects can indeed introduce in solid NMR of quadrupole nuclei shifts that are in the order of several kHz, yet they will not affect symmetric single- or multiple-quantum $-m\leftrightarrow+m$ transitions and will only show up on single-quantum spectra when these arise from satellite transitions. Even then, this new effect leads to line shape distortions that are difficult to discern when dealing with static random powders due to the presence of much larger first order anisotropies. Upon executing MAS these effects do actually become discernible for the Q-CSA cross-correlations, yet vanish altogether for the lower-ranked Q-ACS terms. Hence the best chance for detecting quadrupolar-ACS cross-correlations is based on single-crystal NMR spectroscopy.[1,22] To achieve this kind of observation a single-crystal NMR probe was built, and employed in repetitive measures of the central- and satellite-transition rotation patterns arising from ^{59}Co (an $I=7/2$ nucleus) in a model octahedral cobalt complex. These data were then analyzed with a Simplex numerical fitting algorithm which took into account first and second order quadrupole effects, secular and nonsecular shielding contributions, as well as potential random and systematic errors. The ACS parameters assessed from these measurements for the ^{59}Co sites were in the order of 100–1000 ppms.

II. SECOND ORDER SHIELDING-QUADRUPOLE EFFECTS

A. Derivation of the analytical higher order Hamiltonians

Although an evaluation of nonsecular shielding effects on the transitions of an I^{-} 1 spin can be carried out by numerical diagonalization of the complete laboratory-frame Hamiltonian, it is illustrative to derive their description via a perturbative approach. Toward this end we consider the laboratory frame single-spin Hamiltonian

$$H_{\text{lab}}=H_Z+H_Q+H_{\text{CS}}+H_{\text{ACS}}, \tag{2}$$

where H_Z is the dominant Zeeman coupling of the spin with the external magnetic field, H_Q is its quadrupolar interaction, and for clarity's sake we express the chemical shift interaction as the sum of H_{CS} (the $l=0,2$ parts of the shielding tensor) and of H_{ACS} (the $l=1$ part). To exploit the symmetry properties of these interactions it is best to represent them using irreducible spherical tensor operators as

$$\begin{aligned}
&H_Z=-\gamma B_0 I_z=\omega_0 T_{1,0},\\
&H_Q=\sum_{m=-2}^{2}(-1)^m T^Q_{2,-m}R^Q_{2,m},\\
&H_{\text{CS}}=\gamma\delta_{\text{iso}}B_0 I_z+\sum_{m=-2}^{2}(-1)^m T^{\text{CS}}_{2,-m}R^{\text{CS}}_{2,m},\\
&H_{\text{ACS}}=\sum_{m=-1}^{1}(-1)^m T^{\text{ACS}}_{1,m}R^{\text{ACS}}_{1,-m}.
\end{aligned} \tag{3}$$

The spin parts of the various Hamiltonians are defined as

$$\begin{aligned}
&T^Q_{2,0}=\chi_Q[3I_z^2-I(I+1)],\\
&T^Q_{z,\pm1}=\mp\sqrt{\frac{3}{2}}\chi_Q(I_zI_\pm+I_\pm I_z),\quad T^Q_{2,\pm2}=\sqrt{\frac{3}{2}}\chi_Q I_\pm^2,
\end{aligned} \tag{4}$$

$$T^{\text{CS}}_{2,0}=\sqrt{\frac{2}{3}}I_zB_0,\ \ T^{\text{cs}}_{2,\pm1}=\mp\frac{1}{2}I_\pm B_0,\ \ T^{\text{CS}}_{2,\pm2}=0, \tag{5}$$

and

$$T^{\text{ACS}}_{1,0}=0,\ \ T^{\text{ACS}}_{1,\pm1}=-\tfrac{1}{2}I_\pm B_0. \tag{6}$$

Here χ_Q represents the quadrupolar coupling parameter, and the spatial components $\{R^\lambda_{l,m}\}_{\lambda=Q,\text{CS,ACS}}$ are given in further detail below. An explicit expression of the laboratory-frame Hamiltonian in Eq. (2) is therefore

$$H=\omega_0 I_z+\chi_Q\left[\begin{array}{c}\sqrt{\frac{3}{2}}R^Q_{2,-2}I_+^2-\sqrt{\frac{3}{2}}R^Q_{2,-1}\{I_zI_++I_+I_z\}+R^Q_{2,0}\{3I_z^2-I(I+1)\}\\ +\sqrt{\frac{3}{2}}R^Q_{2,1}\{I_zI_-+I_-I_z\}+\sqrt{\frac{3}{2}}R^Q_{2,2}I_-^2\end{array}\right]$$
$$+\left(\gamma\delta_{\mathrm{iso}}+\sqrt{\frac{2}{3}}R^{\mathrm{CS}}_{2,0}\right)B_0I_z+\frac{1}{2}R^{\mathrm{CS}}_{2,-1}B_0I_+-\frac{1}{2}R^{\mathrm{CS}}_{2,1}B_0I_-+\frac{1}{2}R^{\mathrm{ACS}}_{1,-1}B_0I_++\frac{1}{2}R^{\mathrm{ACS}}_{1,1}B_0I_-. \tag{7}$$

Physical insight into the effects that the various couplings will have on an NMR experiment can be retrieved if all internal Hamiltonians H_λ are treated as perturbations to the dominant Zeeman term. A common approach to calculate the effective Hamiltonians resulting in this high-field regime involves removing the Zeeman term by going into an interaction representation driven by the propagator

$$U(t)=\exp[-i\omega_0 I_z t], \tag{8}$$

which imparts into each H_λ the time dependence

$$\tilde{H}_\lambda(t)=U(t)\cdot H_\lambda\cdot U^{-1}(t)+\frac{dU(t)}{dt}U^{-1}(t). \tag{9}$$

The resulting time-dependent expressions are

$$\tilde{H}_Q(t)=\frac{\sqrt{6}}{2}\chi_Q\left\{\begin{array}{c}\frac{2}{\sqrt{6}}R^Q_{2,0}\{3I_z^2-I(I+1)\}+R^Q_{2,-1}I_+(2I_z+1)e^{i\omega_0 t}-R^Q_{2,1}I_-(2I_z-1)e^{-i\omega_0 t}\\ +R^Q_{2,-2}I_+^2e^{2i\omega_0 t}+R^Q_{2,2}I_-^2e^{-2i\omega_0 t}\end{array}\right\} \tag{10}$$

for the quadrupolar Hamiltonian,

$$\tilde{H}_{\mathrm{CS}}(t)=\left(\delta_{\mathrm{iso}}\omega_0+\frac{2}{\sqrt{6}}B_0R^{\mathrm{CS}}_{2,0}\right)I_z+\frac{1}{2}B_0R^{\mathrm{CS}}_{2,-1}I_+e^{i\omega_0 t}-\frac{1}{2}B_0R^{\mathrm{CS}}_{2,+1}I_-e^{-i\omega_0 t} \tag{11}$$

for the symmetric chemical shift contributions, and

$$\tilde{H}_{\mathrm{ACS}}(t)=\tfrac{1}{2}B_0R^{\mathrm{ACS}}_{1-1}I_+e^{i\omega_0 t}+\tfrac{1}{2}B_0R^{\mathrm{ACS}}_{1+1}I_-e^{-i\omega_0 t} \tag{12}$$

for the ACS. Average Hamiltonian theory can then be applied to obtain a time-independent rendering of these rotating-frame interactions according to[1,23]

$$\bar{H}=H^{(1)}+H^{(2)}+\cdots, \tag{13}$$

where

$$H^1_\lambda=\frac{1}{\tau_c}\int_0^{\tau_c}\tilde{H}_\lambda(t)dt, \tag{14a}$$

$$H^{(2)}_{\lambda,\lambda'}=\frac{-i}{2\tau_c}\int_0^{\tau_c}dt\int_0^t[\tilde{H}_\lambda(t),\tilde{H}_{\lambda'}(t')]dt', \tag{14b}$$

and $\tau_c\approx 2\pi/\omega_0$ is the Larmor period. The frequencies of NMR transitions can usually be calculated with enough accuracy by considering only the first order term for the chemical shift, plus the first and second order terms for the quadrupolar coupling. This leads to the well known expressions

$$H^{(1)}_{\mathrm{CS}}=\left(\delta_{\mathrm{iso}}\omega_0+\frac{2}{\sqrt{6}}B_0R^{\mathrm{CS}}_{2,0}\right)I_z, \tag{15}$$

$$H^{(1)}_Q=\chi_QR^Q_{2,0}\{3I_z^2-I(I+1)\}, \tag{16}$$

$$H^{(2)}_{Q,Q}=\frac{3}{\omega_0}\chi_Q^2\{R^Q_{2,-1}R^Q_{2,1}I_z[4I(I+1)-8I_z^2-1]+R^Q_{2,-2}R^Q_{2,2}I_z[2I(I+1)-2I_z^2-1]\}. \tag{17}$$

The case under consideration, however, assumes that the quadrupolar and shielding couplings are large enough to warrant the consideration of quadrupolar-shielding cross terms $H^{(2)}_{Q,\lambda}$. The inclusion of all such possible second order terms involving $\tilde{H}_{\mathrm{CS}}$ and $\tilde{H}_{\mathrm{ACS}}$ into Eq. (14b) leads to

$$H^{(2)}_{Q,\mathrm{CSA}}=-\sqrt{\frac{3}{2}}\chi_Q\frac{B_0}{\omega_0}(R^Q_{2,1}R^{\mathrm{CS}}_{2,-1}+R^Q_{2,-1}R^{\mathrm{CS}}_{2,1})\times\{3I_z^2-I(I+1)\}, \tag{18}$$

$$H^{(2)}_{Q,\mathrm{ACS}}=-\sqrt{\frac{3}{2}}\chi_Q\frac{B_0}{\omega_0}(R^Q_{2,1}R^{\mathrm{ACS}}_{1,-1}-R^Q_{2,-1}R^{\mathrm{ACS}}_{1,1})\times\{3I_z^2-I(I+1)\}. \tag{19}$$

These interactions possess the basic features adumbrated in the Introduction: they are proportional to χ_QB_0/ω_0 and therefore independent of the external magnetic field strength, while magnitude-wise they are given by ppms of the quadrupolar coupling. Also interesting to note is the quadratic dependence characterizing the spin parts of these second order interactions, which predicts that they will not affect the transition frequencies of either the central or any other symmetric transitions within the spin manifold.

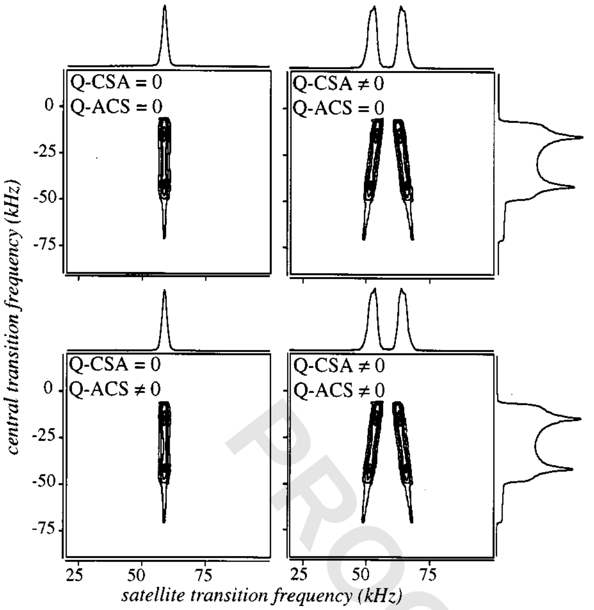

FIG. 1. 2D satellite/central transition correlation spectra of an $I=7/2$ nucleus undergoing MAS, upon including the second order Q-CSA interaction (left panels) and the Q-ACS interaction (bottom panels). In all cases the outermost transition ($\pm 5/2 \leftrightarrow \pm 7/2$) was assumed monitored, and a shearing transformation that ideally produces an isotropic/second order quadrupole correlation was applied on all the spectra. Parameters involved: $\omega_0/2\pi = 80$ MHz, $\chi_Q/2\pi = 0.71$ MHz, $\eta_Q = 0.2$, $\delta_{\text{iso}} = 0$ ppm, $\delta_{\text{CS}} = 1500$ ppm, $\eta_{\text{CS}} = 0.3$, $\delta^a_{XY} = \delta^a_{ZX} = \delta^a_{ZY} = 1000$ ppm, $(a,b,c) = (0°,0°,0°)$ (coinciding quadrupole and CS tensors).

B. Higher order shielding effects on spinning and static spectra

The overall resemblance between these second order shielding-quadrupolar effects and those arising in heteronuclear dipolar-quadrupolar cross-correlations,[15,24] suggests that, just as in this latter case, quadrupole effects might enable the observation of nonsecular shielding terms through direct solid state NMR experiments. To further explore this possibility it is necessary to elaborate on the nature of the spatial components in Eqs. (18)–(19). In their principal axes systems (PASs), these elements are given by the spatial-space analogs of Eqs. (4)–(6):[1]

$$\rho^Q_{2,0} = \frac{1}{2} V^Q_{ZZ} = \frac{1}{2} eq, \quad \rho^Q_{2,\pm 1} = 0,$$
$$\rho^Q_{2,\pm 2} = \frac{1}{2\sqrt{6}} (V^Q_{XX} - V^Q_{YY}) = \frac{eq}{2\sqrt{6}} \eta_Q, \tag{20}$$

$$\rho^{\text{CS}}_{2,0} = \sqrt{\frac{3}{2}} \gamma_i \delta_{\text{CS}}, \quad \rho^{\text{CS}}_{2,\pm 1} = 0, \quad \rho^{\text{CS}}_{2,\pm 2} = \frac{1}{2} \gamma_i \eta_{\text{CS}} \delta_{\text{CS}}, \tag{21}$$

$$\rho^{\text{ACS}}_{1,0} = -\sqrt{2i}\, \gamma_i \delta^a_{XY}, \quad \rho^{\text{ACS}}_{1,\pm 1} = \gamma_i (\delta^a_{XZ} \pm i\, \delta^a_{YZ}), \tag{22}$$

with Eqs. (21), (22) relying on conventional spin-based definitions of displacements δ_{ij} respective to a standard defining the chemical shift scale. The spherical tensor elements $\{R^{\lambda}_{l,m}\}_{\lambda = Q,\text{CS,ACS}}$ involved in the high-field Hamiltonians $H^{(2)}_{Q,\lambda}$ can then be related to these PAS expressions via a series of consecutive transformations into the laboratory reference frame. In the present work we define these according to sets of Euler angles

$$\left.\begin{matrix}\text{CS}\\ \text{ACS}\end{matrix}\right\} \xrightarrow{(a,b,c)} Q \xrightarrow{(\alpha,\beta,\gamma)} \left.\begin{matrix}GON\\ ROT\end{matrix}\right\} \xrightarrow{(\phi,\theta,0° \text{ or } w_r t, 54.7°, 0°)} LAB. \tag{23}$$

This model contemplates two alternative experiments: one involving a goniometer-based single-crystal measurement where a tenon frame defined by (ϕ, θ, 0°) is systematically varied, and another a rotor-based MAS line shape

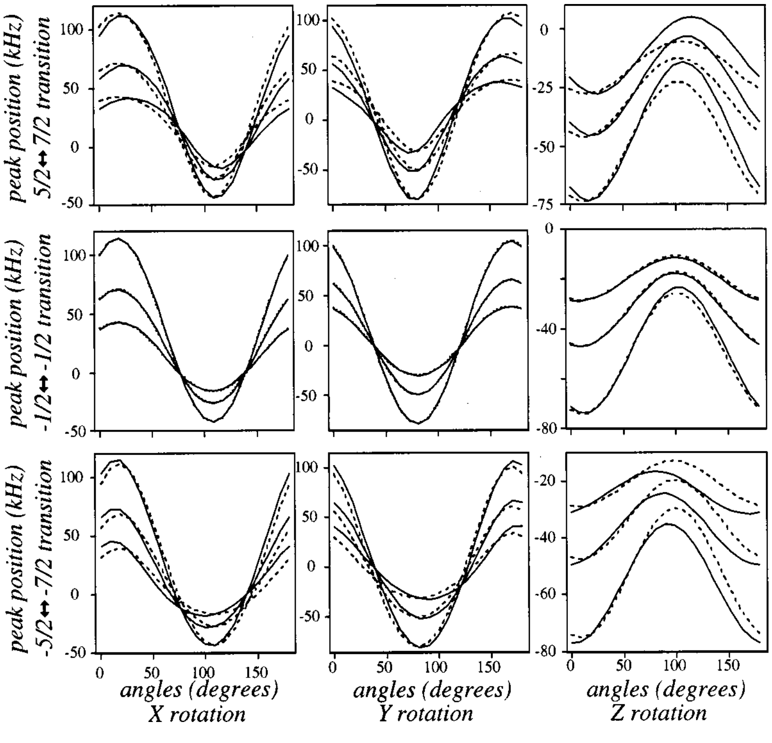

FIG. 2. Orthogonal set of single-crystal rotation patterns expected from the indicated $m-l \leftrightarrow m$ transitions for an $I=7/2$ nucleus. Curves were calculated with and without the inclusion of quadrupolar-ACS cross-correlation effects, at three different Larmor frequencies within each inset: $\omega_0/2\pi = 30$ MHz (top traces), 50 MHz (middle traces), and 30 MHz (bottom traces); all other coupling parameters involved are as in Fig. 1. For the sake of clarity only the following interactions were included in these plots: $H^{(1)}_{\text{CS}} + H^{(2)}_{Q\text{-CS}}$ (- - - -), $H^{1}_{\text{CS}} + H^{(2)}_{Q\text{-Cs}} + H^{(2)}_{Q\text{-ACS}}$ (– – – –). Notice the negligible quadrupolar-ACS effects on $-m \leftrightarrow +m$ transitions and the invariance of these effects on the magnetic field strength.

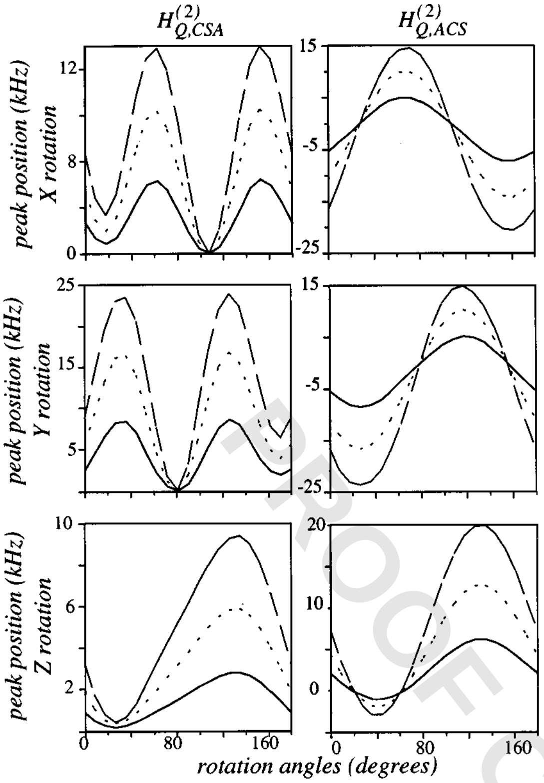

FIG. 3. Periodicities expected from quadrupole-CSA and quadrupole-ACS effects for different peak combinations within an $I=7/2$ manifold, chosen so as to remove first order shielding effects: $v_{3/2\leftrightarrow 1/2}-v_{-1/2\leftrightarrow -3/2}$ (– – –); $v_{5/2\leftrightarrow 3/2}-v_{-3/2\leftrightarrow -5/2}$ (- - - -); $v_{7/2\leftrightarrow 5/2}-v_{-5/2\leftrightarrow -7/2}$ (— — —). All the interactions and parameters involved in these calculations are as in Fig. 2, with $\omega_0/2\pi=30$ MHz.

analysis where interactions become time dependent. In either case the Euler set (a, b, c) relating shielding and quadrupolar PASs is fixed in the molecule, whereas the (α, β, γ) angles are determined in single-crystal but have to be integrated over a solid sphere in powder cases. Regardless of the experiment chosen, all spatial components appearing in the interaction Hamiltonians of Eq. (14) can be computed from these rotations according to

$$R^{Q}_{2,m}=\sum_{n=-2}^{2} D^{2}_{n,m}\left(\begin{array}{c}\phi,\theta,0^\circ\\ \text{or}\\ \omega_r t,54.7^\circ,0^\circ\end{array}\right)\sum_{k=-2}^{2} D^{2}_{k,n}(\alpha,\beta,\gamma)\rho^{Q}_{2,k}, \tag{24}$$

$$R^{\mathrm{CS}}_{2,m}=\sum_{n=-2}^{2} D^{2}_{n,m}\left(\begin{array}{c}\phi,\theta,0^\circ\\ \text{or}\\ \omega_r t,54.7^\circ,0^\circ\end{array}\right)\sum_{k=-2}^{2} D^{2}_{k,n}(\alpha,\beta,\gamma)\times\sum_{p=-2}^{2} D^{2}_{p,k}(a,b,c)\rho^{\mathrm{CS}}_{2,p}, \tag{25}$$

$$R^{\mathrm{ACS}}_{1,m}=\sum_{n=-1}^{1} D^{1}_{n,m}\left(\begin{array}{c}\phi,\theta,0^\circ\\ \text{or}\\ \omega_r t,54.7^\circ,0^\circ\end{array}\right)\sum_{k=-1}^{1} D^{1}_{k,n}(\alpha,\beta,\gamma)\times\sum_{p=-1}^{1} D^{1}_{p,k}(a,b,c)\rho^{\mathrm{ACS}}_{1,p}, \tag{26}$$

where in quadrupolar and CS cases $m=0$, ± 1, ± 2, and for the ACS $m=0,\pm 1$.

These expressions enable one to assess the spectral changes that quadrupolar-CSA and quadrupolar-ACS effects will introduce, and then deduce whether such changes could enable the direct determination of the antisymmetric contributions. Toward this end we considered a hypothetical case incorporating favorable coupling parameters characteristic of a transition metal isotope:[25,26] $I=7/2$, $\chi_Q/2\pi=0.71$ MHz, $\delta_{\mathrm{iso}}=0$ ppm, $\delta_{\mathrm{CS}}=1500$ ppm, $\delta^{a}_{XY}=\delta^{a}_{XZ}=\delta^{a}_{YZ}=1000$ ppm. In order to consider the variations in the MAS NMR line shapes that can be expected upon factoring in the nonsecular shielding effects we use the Hamiltonians in Eqs. (18)–(19), the time-dependent spatial components $\{R^{\lambda}_{2,m},R^{\mathrm{ACS}}_{1,m}\}$ resulting from Eqs. (24)–(26), and consider for simplicity the rotational time averages corresponding to sideband-free observations that are stroboscopic with MAS. No influences are then visible in the central $1/2\leftrightarrow -1/2$ spectra, yet these simulations also show noticeable distortions on the satellite transitions that arising from CSA-quadrupolar correlations cannot be entirely averaged away by MAS. In order to better appreciate such effects we consider a rotor-synchronous sampling (which effectively eliminates $H^{(1)}_{Q}$ and $H^{(1)}_{\mathrm{CS}}$ effects), as well as a 2D rather than a 1D NMR experiment where satellite line shapes are correlated with those of the central transition. A shearing transformation along the lines of multiple-quantum or satellite-transition MAS acquisitions.[27,28] compensates then for $H^{(2)}_{Q,Q}$ effects along one of the spectral dimensions and leaves only the higher order, partially averaged effects on which we are here interested. The top panels of Fig. 1 shows how the originally sharp satellite transition MAS line shape then changes upon introducing a CSA. Unlike other fourth-rank broadenings such as those arising from quadrupolar-dipolar or quadrupolar-quadrupolar cross-correlations, these broadenings should have the peculiarity that they will not sharpen as the magnetic field increases. Further insight on the influence of these effects on single- and multiple-quantum MAS experiments on half-integer quadrupoles will be discussed elsewhere. By contrast to these CSA driven effects, the spatial anisotropies involved in the quadrupolar-ACS Hamiltonian are of rank <4 and thus susceptible to be averaged away by rapid MAS (Fig. 1, top vs bottom panels). These effects will still affect the satellite-transition patterns observed in static powders, yet as mentioned these are minor intensity changes and thus unlikely to enable a direct measurement of the antisymmetric shielding components.

In view of this poor prognosis toward the direct measurement of the antisymmetric chemical shieldings, we decided to explore the results that may arise when probing these interactions via single-crystal NMR analyses. Figure 2 shows the rotation patterns that can then be expected for various $I=7/2$ transitions, with and without the inclusion of quadrupolar-ACS cross-correlation effects. These rotation plot calculations now evidence several positive features including effects that are large enough to enable measurement of the ACS components, and a distinctive magnification of the ACS effects for the outer satellite transitions. Also worth noting is the different periodicities that quadrupole-CS and

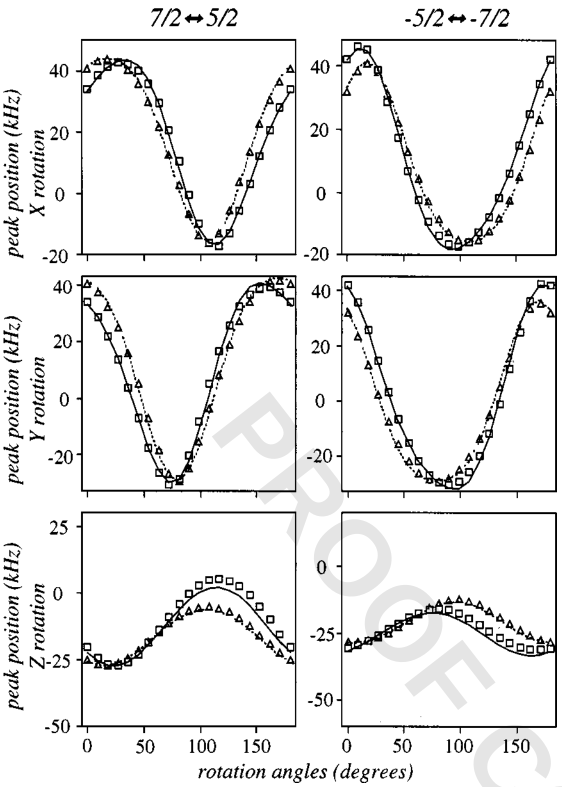

FIG. 4. Comparisons between the results afforded by exact numerical calculations (lines) vis-a-vis analytical predictions (symbols) of CSA and Q-CSA effects in the absence (△,---) and upon including (□,—) Q-ACS cross-correlations. Analytical predictions are based on the first and second order Hamiltonians described in the text; coupling parameters were in all cases as described in Fig. 3.

quadrupole-ACS effects display in their single-crystal rotation plots (Fig. 3): the former shows higher-frequency oscillations, as a result of the higher ranks involved in its spatial coupling components.

C. Comparison with exact numerical calculations

These results suggest the feasibility of a direct determination of the ACS components based on goniometric, single-crystal NMR measurements on quadrupoles. Before embarking on this, however, it is worth comparing the predictions that the analytical model used to derive such conclusion makes against expectations arising from full numerical diagonalizations of the exact Hamiltonian. Calculating peak positions from the latter involves expressing the laboratory-frame Hamiltonian [Eq. (7)] in the basis set of the I_z angular momentum operator, and employing the spatial rotations in Eqs. (24)–(26) to derive the frequency values of the different couplings. NMR frequencies can then be extracted from the differences between the eigenvalues resulting after diagonalizing the total Hamiltonian. A comparison between the exact transition frequencies that results from these numerical calculations and the predictions of the first and second order Hamiltonians derived above is present in Fig. 4. The rms deviations between the frequency positions predicted by both models under the indicated conditions is less than 100 Hz. It is thus clear that the insight provided by the perturbative equations can be used as an excellent starting point for quantitative nonsecular shielding evaluations.

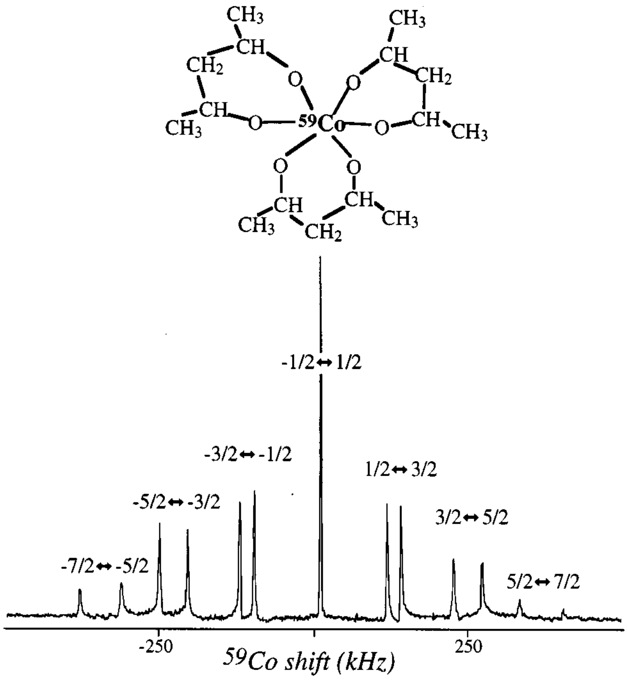

FIG. 5. Top: Structure of Cobalt (III) acetylacetonate, the complex targeted in this work. Bottom: Typical ^{59}Co NMR spectrum obtained throughout this single-crystal rotation study of Co$(acac)_3$, denoting the various transitions involved for the two magnetically inequivalent sites in the monoclinic unit cell.

III. DATA COLLECTION AND ANALYSIS

It follows from the arguments above that single-crystal NMR on the satellite transitions of a quadrupolar nucleus could yield direct spectral insight into nonsecular quadrupole-shielding cross correlations in general, and into the magnitude of ACS components in particular. Two types of nuclei were initially targeted for such measures: ^{59}Co, an $I=7/2$ nucleus, and ^{55}Mn, an $I=5/2$ spin. Both of these elements are transition metals subject to sizable chemical shielding that can potentially exceed 10^4 ppm, possess a moderate nuclear quadrupole moments (0.38 and 0.4 barns, respectively) that may result in MHz-sized χ_Q couplings, and have both been targets of detailed single crystal studies.[25,26,29,30] Unfortunately, out of the various compounds assayed for this project, only one of them yielded crystals of sufficiently high quality to display all satellite transitions at any orientations with respect to B_0: cobalt(II)tris(acetylacetonate) [Co(acac)$_3$, Fig. 5]. Single-and poly-crystalline samples of these compound have already been the subject of powder and single-crystal ^{59}CoNMR studies;[31–33] for the sake of our satellite transition observations their crystals were obtained by slow evaporation of an acetone solution at room temperature. The resulting well-defined prisms belonged to space group $P2_1/c$, and contained four molecules per unit cell related to one another by symmetry operations.[34]

Two inequivalent sets of signals where thus observed for each of the seven single-quantum transitions in the manifold. To carry out the actual study a single-crystal NMR probe was designed and built based on the highly accurate model of Jakobsen and co-workers.[35] The resulting open-faced goniometer system achieved an angular accuracy better than 0.02° for either X, Y, or Z rotations perpendicular to the magnetic field, and although its filling factor is small this was compensated by the high sensitivity of ^{59}Co and by a short relaxation time that enabled a fast repetitive pulsing. Out of the several orthogonal rotation studies that were performed, the results presented below stem from six complete sets of 240° rotations on $\approx 1.5\times 1.0\times 2.0$ mm crystals. These crystals were glued on a tenon fitting into the X, Y, and Z dovetails of the goniometer, locked in turn inside the probehead detection coil. The NMR probe itself was bolted to the room temperature shims of the 11.8 T magnet, where all determinations took place at a ca. 119 MHz ^{59}Co Larmor frequency. This rigid setup enabled a high reproducibility; on disassembling and remounting the complete probehead system, signal displacements smaller than 1 kHz were repetitively observed for the outermost ^{59}Co transitions. Thirty-four spectra separated by angular increments of 7.14° were collected for each of the orthogonal rotation axes, which for the sake of literature consistency are denoted here as $-X^T, Y^T - Z^T$.[35,36] All of these acquisitions were carried out at a stabilized temperature of 30 °C using a laboratory-built NMR spectrometer and temperature controller. Each spectrum collected 1024 scans separated by 1 s using a 1 MHz spectral window and a 2 μs rf excitation ($\gamma B_1 = 55$ kHz). When needed, several acquisitions separated by 1 MHz offsets were combined in order to create a sufficiently large spectral window (≈2.5 MHz) to accommodate all satellite transition peaks.

To fit the various coupling and angular parameters defining the single-crystal spectra, sites were identified first in the different rotation patterns according to their need to fulfill the coincidence relations $-X^T(0°) = Y(0°)$, $-X^T(90°) = -Z^T(90)$ and $Y^T(90) = -Z^T(0)$.[22,36] In order to analyze the combined rotation plots of all the single-quantum transitions the perturbative treatment of the preceding section was then employed. It then follows from Eqs. (15)–(19) that the energies defining each of the high field I-spin eigenstates m, $-l \leqslant m \leqslant l$, will be given by

$$E(m) = (\Pi + \Lambda + \mathrm{X})[3m^2 - I(I+1)] + \Delta \cdot m + \Phi^{(1)}\{m[2I(I+1) - 2m^2 - 1]\} + \Phi^{(2)}\{m[4I(I+1) - 8m^2 - 1]\}. \tag{27}$$

Here Π denotes the first order quadrupolar frequency, Δ the first order chemical shielding, $\Phi^{(1,2)}$ are two terms related to the second order quadrupole effects, and Λ, X are the quadrupolar-CSA and quadrupolar-ACS cross correlations being sought. With this formula the perturbative expressions for the seven single-quantum transitions of an $I = 7/2$ nucleus can be derived as

$$\nu(m \leftrightarrow m-1) = \begin{cases} 18(\Pi + \Lambda + \mathrm{X}) + \Delta - 24\Phi^{(1)} - 156\Phi^{(2)}, & \text{for } m = 7/2 \\ 12(\Pi + \Lambda + \mathrm{X}) + \Delta + 6\Phi^{(1)} - 36\Phi^{(2)}, & \text{for } m = 5/2 \\ 6(\Pi + \Lambda + \mathrm{X}) + \Delta + 24\Phi^{(1)} + 36\Phi^{(2)}, & \text{for } m = 3/2 \\ \Delta + 30\Phi^{(1)} + 60\Phi^{(2)}, & \text{for } m = 1/2 \\ -6(\Pi + \Lambda + \mathrm{X}) + \Delta + 24\Phi^{(1)} + 36\Phi^{(2)}, & \text{for } m = -1/2 \\ -12(\Pi + \Lambda + \mathrm{X}) + \Delta + 6\Phi^{(1)} - 36\Phi^{(2)}, & \text{for } m = -3/2 \\ -18(\Pi + \Lambda + \mathrm{X}) + \Delta - 24\Phi^{(1)} - 156\Phi^{(2)}, & \text{for } m = -5/2 \end{cases}. \tag{28}$$

Notice that since X has the same spin dependence as the first order quadrupole effect (even if a different spatial one), an accurate knowledge of this coupling is essential for the ACS determination.

Equation (28) was used as a starting point for analyzing the experimental single-crystal NMR data. The actual algorithm employed in the study for analyzing the data is depicted in Fig. 6. Its first stage involved estimating the quadrupolar parameters by ignoring all higher order effects, and relying only on differences

$$\Delta\nu(m) = \nu(m \leftrightarrow m-1) - \nu(-(m-1) \leftrightarrow m) \tag{29}$$

between satellite transitions, assumed to contain solely first order quadrupole effects. In the goniometer frame these differences can be written as a function of the angle of the crystal rotation Θ by the standard dependence[1,22]

$$\Delta\nu(m) = A_m^{Q,1} + B_m^{Q,1}\cos 2\Theta + C_m^{Q,1}\sin 2\Theta. \tag{30}$$

The exact definitions of these three coefficients, extracted for each $-X^T, Y^T, -Z^T$ rotation plot by least square fittings, are given in the Appendix. Their determination afforded an initial estimate for the values and orientations of the quadrupolar tensors. Next, the central transition and sums of satellite transition frequencies

$$\Sigma\nu(m) = \nu(m \leftrightarrow m-1) + \nu(-(m-1) \leftrightarrow m) \tag{31}$$

were combined to derive frequency expressions free from first order quadrupole effects. These allowed us to define the chemical shift couplings, as well as further refinements on the quadrupole parameters via an analysis of the second order effects they contain. The former were fit by a three term expression in the style of Eq. (30), whereas the latter were extracted from the characteristic second order dependence[36,37]

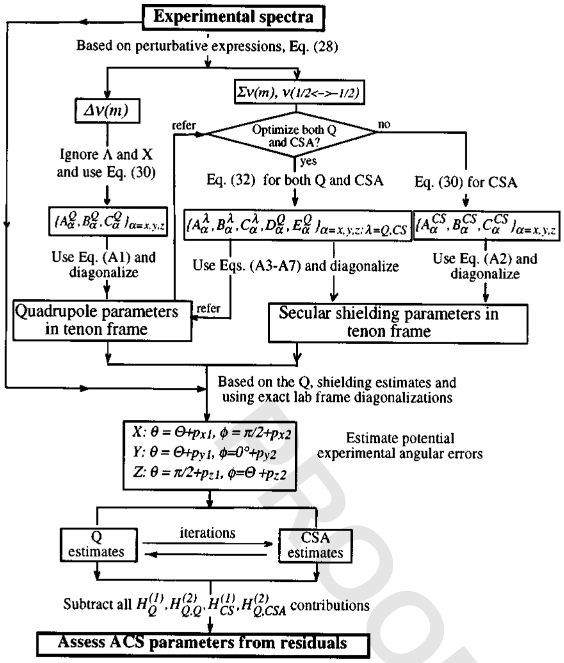

FIG. 6. Schematic flow diagram of the data fitting procedures employed in this work. throughout the fits the conventions $|V_{zz}^{Q}|\geqslant|V_{yy}^{Q}|\geqslant|V_{xx}^{Q}|$ and $\delta_{\mathrm{CS}}=\delta_{zz}-\delta_{\mathrm{iso}}$, $\eta_{\mathrm{CS}}=(\delta_{yy}-\delta_{xx})/\delta_{\mathrm{CS}}$, $\delta_{\mathrm{iso}}=(\delta_{xx}+\delta_{yy}+\delta_{zz})/3$, $|\delta_{zz}-\delta_{\mathrm{iso}}|\geqslant|\delta_{yy}-\delta_{\mathrm{iso}}|\geqslant|\delta_{xx}-\delta_{\mathrm{iso}}|$ were assumed for the quadrupolar and shielding tensors respectively. Further details on the individual fitting procedures are given in the text.

$$\Sigma\,\nu(m)=A_{m}^{Q,2}+B_{m}^{Q,2}\cos 2\Theta+C_{m}^{Q,2}\sin 2\Theta$$
$$+D_{m}^{Q,2}\cos 4\Theta+E_{m}^{Q,2}\sin 4\Theta. \qquad (32)$$

Further definitions of these shielding and quadrupolar coefficients are given in the Appendix.

The following stage of the data analysis relied on employing these approximate quadrupolar and secular shielding parameters, in a further refinement of the complete single-crystal data set that also incorporates ACS components. Toward this end a Simplex numerical algorithm was developed,[38] which relied on the pre-estimated quadrupole and CS values as starting parameters but carried now an exact diagonalization of the full laboratory-frame Hamiltonian in order to simultaneously optimize all the couplings involved. This algorithm relied on a minimization of the χ-square parameters of the fit, and gave consistently good results when tested on synthetic data to which random frequency shifts in the order of 1–5 kHz had been added. The results obtained with it for the experimental Co($acac$)$_3$ measurements are presented below.

IV. RESULTS AND DISCUSSION

A summary of typical ^{59}Co NMR rotation plots, depicting the experimental frequencies collected as a function of the goniometer's orientation for all transitions in the two magnetically inequivalent sites of a Co($acac$)$_3$ single crystal, is shown in Fig. 7. Though time consuming, such measurements were carried out twice in order to improve the statistics of the χ-square fitting. These data were then merged together for processing into the $\Delta\upsilon$ and $\Sigma\upsilon$ combinations described earlier, from which quadrupolar and CS parameters were extracted. The resulting experimental sets together with their best fits are shown in Fig. 8; a summary of the various $\{A_{\alpha}^{\lambda},B_{\alpha}^{\lambda},C_{\alpha}^{\lambda}\}_{\alpha=x,y,z;\lambda=Q,\mathrm{CS}}$ coefficients resulting from these fits is given in Table I. From these coefficients it is possible to extract the secular quadrupolar and shielding tensors elements relative to the tenon-frame, and then in turn the values and Euler angles characterizing their respective PAS components. A summary of the former, together with the relative orientation resulting between the tensors, is listed in Table II. Also shown for comparison are the very similar values that solely on the basis of the central transition rotation plots were recently obtained by Wasylishen and coworkers for the same compound.[33]

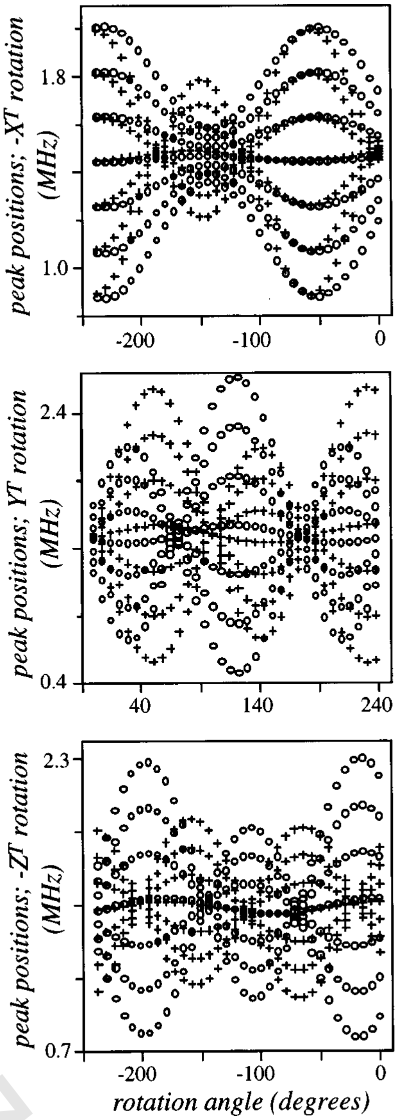

FIG. 7. ^{59}Co NMR peak positions [with respect to 1M aq. K$_3$Co(CN)$_6$] observed for one of the Co($acac$)$_3$ single-crystal rotation plots at 11.8 T as a function of the goniometer position with respect to the external magnetic field. Site assignments were performed using the peak coincidences at $-X^{T}(0°)=Y(0°)$, $-X^{T}(90°)=-Z^{T}(90°)$ and $Y^{T}(90°)=-Z^{T}(0°)$: (○) symbolizes signals from site 1; (+) symbolizes site 2.

Although within the vertical scale with which Fig. 8 is plotted the agreement between experiment and fit looks

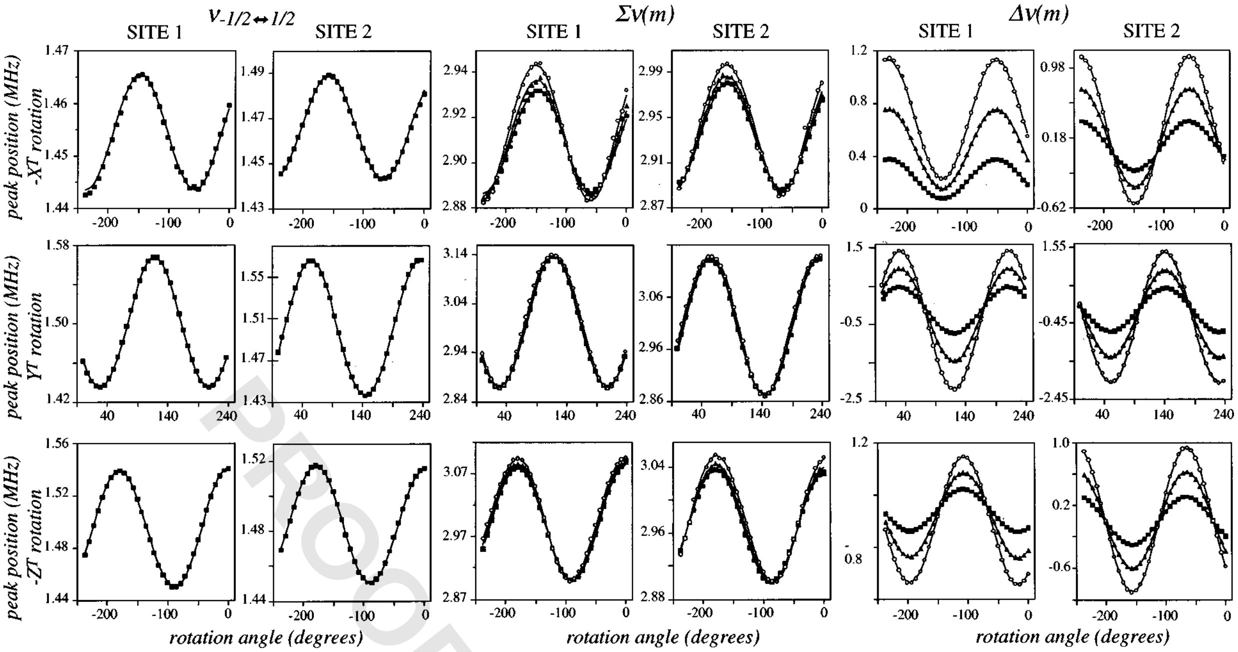

FIG. 8. Experimental peak positions (symbols) and best fit results (lines) obtained from a representative rotation study of the central (left), satellites' sum (center), and satellites' difference (left) transitions of Co$(acac)_3$. For the satellites' combination data, symbols represent $v_{7/2\leftrightarrow5/2}\pm v_{-5/2\leftrightarrow-7/2}$ (○), $v_{5/2\leftrightarrow3/2}\pm v_{-3/2\leftrightarrow-5/2}$ (▲) and $v_{3/2\leftrightarrow1/2}\pm v_{-1/2\leftrightarrow-3/2}$ (■).

nearly perfect, there is still at this stage an rms deviation of ca. 10^4 Hz between these two sets of data. It is within these relatively small deviations that the ACS and other nonsecular components are to be sought. Before doing so, however, we considered at this stage the potentially distortions that could arise from experimental angular errors. Throughout the single-crystal measurements these could have originated from two different sources: systematic and random. The latter are mainly associated to uncertainties in locating the exact peak positions, and varied between ≈200 Hz for the central to ≈4000 Hz for the outermost single-quantum transitions. These errors were partly compensated by having at our disposal two independent data measurements plus data from two inequivalent sites, via the χ-square statistical analysis. As for systematic errors these could be traced to displacements of all angular readings coming from backlash in the goniometer's gear mechanism, from potential nonorthogonalities of the (X^T,Y^T,Z^T) tenon dovetails, or from a tilt of the probe inside the magnet's bore resulting in nonorthogonal rotations with respect to the B_0 field. The first of these complications could be accurately dealt with by carrying out all of the goniometer's rotations in the same direction; the resulting errors, in frequency terms, were at most a few hundred Hz. The second complication was minimized via accurate machining. The third complication, however, proved the most challenging to correct. Thus in spite of constructing long magnet-bolted sleeves to align the probehead within the field, minor wobbling precessions that departed the axis of rotation from its ideal orthogonality with respect to B_0 could be detected. To deal simultaneously with the last two types of systematic errors we thus decided to include into the fit, still at the secular coupling level, potential azimuthal, and longitudinal deviations. These would distort the ideal analysis of rotation Eqs. (30), (32) according to

$$-X^T \text{ rotation: } \theta=-\Theta+p_1^x,\quad \phi=\pi/2+p_2^x,$$

$$Y^T \text{ rotation: } \theta=\Theta+p_1^y,\quad \phi=0^\circ+p_2^y, \tag{33}$$

TABLE I. First order coefficients resulting from the least-square fit (six iterations) of the ^{59}Co single-crystal splittings for site 1 and 2 of Co$(acac)_3$

Quadrupolar			Shielding		
Parameter (Hz)	site 1	site 2	Parameter (Hz)	site 1	site 2
A_x^Q	2.261×10^5	8.78×10^4	A_x^{CS}	1.4547×10^6	1.4668×10^6
B_x^Q	-2.498×10^4	-1.053×10^5	B_x^{CS}	2.98×10^3	1.660×10^4
C_x^Q	-1.486×10^5	-2.633×10^5	C_x^{CS}	9.96×10^3	1.862×10^4
A_y^Q	-1.287×10^5	-1.029×10^5	A_y^{CS}	1.5014×10^6	1.5016×10^6
B_y^Q	3.284×10^5	7.341×10^4	B_y^{CS}	-4.378×10^4	-1.623×10^4
C_y^Q	5.054×10^5	-5.693×10^5	C_y^{CS}	-5.074×10^5	6.374×10^4
A_z^Q	-9.518×10^4	5.9×10^3	A_z^{CS}	1.4958×10^6	1.4848×10^6
B_z^Q	-3.512×10^5	-1.923×10^5	B_z^{CS}	4.610×10^4	3.435×10^4
C_z^Q	2.042×10^5	-2.393×10^5	C_z^{CS}	2.84×10^3	4.79×10^3

TABLE II. ^{59}Co quadrupole couplings (C_Q, η_Q), symmetric parts of chemical shift interactions (δ_{iso}, δ, η_{cs}) and relative orientations (a,b,c) of two tensors for Co($acac$)$_3$

e^2qQ/h (MHz)	η_Q	δ_{iso} (ppm)	δ_{CS} (ppm)[a]	η_{CS}	(a,b,c)[b] (degs)	Ref.
5.53 ± 0.03	0.216 ± 0.003	12500 ± 10	712 ± 5	0.307 ± 0.005	$(-8\pm2, -13\pm2, -4\pm2)$	This work
5.53	0.219	12498	698	0.364	$(7, 8, -27)$	33

[a] Isotropic chemical shift is referenced externally relative to a 1 M of aqueous solution of $K_3Co(CN)_6$.

[b] The relative angles between the quadrupolar and the CSA tensors of other site can be obtained by applying the symmetry operation $(a,-b,c)$.

$$-Z^T \text{ rotation: } \theta=\pi/2+p_1^z, \quad \phi=-\Theta+p_2^z,$$

where Θ is the increment rotation of the tenon, and p_1,p_2 are independent fitting parameters reflecting azimuthal and longitudinal errors. Introducing at this stage of the iterative analysis these angular errors lead to p_1,p_2 values in the 0.1°–0.3° range. This would in turn reflect into a reasonable tilt ($\approx$1 mm) of the probehead's goniometeric assembly from the ideal on-center position. When incorporated into the analysis, these angular errors results in a further decrease in the rms deviation between the experimental and best-fit data of ca. 6 kHz.

These residuals remaining at the conclusion of the fits should reflect the ACS-driven effects, which are the only ones that have yet to be incorporated into the analysis. The rotation plots that then remain after subtracting from the experimental data all these other parameters (Q, CS, Q-CSA, errors effects) are illustrated in Fig. 9, top. Although evidently much of the nature in these rotations is random there are also angular trends in them that should now enable an estimate of the quadrupolar-ACS cross-correlations. These effects were included at this point, and their values optimized through a repetitive iteration that was carried out using both the analytical perturbative expressions as well as full numerical diagonalizations of the laboratory frame Hamiltonian. The ACS values that corresponded to the best-fits yielded the rotational plots illustrated in Fig. 9, bottom. From these it was feasible to extract an estimate of the antisymmetric shielding matrix elements for the ^{59}Co sites in Co($acac$)$_3$: $\delta_{ZX}=1000\pm500$ ppm, $\delta_{ZY}=-1000\pm500$ ppm, $\delta_{XY}=1000\pm1000$ ppm.

V. CONCLUSIONS

The main purposes of the present study were to describe the nature of higher order quadrupolar-shielding effects in solid state NMR, and then explore the feasibility of exploiting these effects in order to directly measure the antisymmetric components of the shielding tensor via single-crystal NMR investigations of quadrupolar nuclei. As part of these tasks a number of analytical Hamiltonians which manifest nonsecular quadrupole-shielding contributions were derived, using average Hamiltonian treatments similar to those employed to derive quadrupole-dipole effects. Main features that were revealed by these expressions include the emergence of field-independent terms, that could be directly traced to nonsecular contributions of either the CSA or the antisymmetric chemical shift. Due to the different ranks involved in the various shielding terms these higher order contributions end up having different properties upon being subjected to MAS, while the fact that these shifts will only affect the satellite spin transitions further complicates their observation. Because of this little chance exists for the measurement of ACS-derived effects from random powders. In order to circumvent this problem, a numerical fitting algorithm capable of extracting these parameters from single-crystal rotation plots—even in the present of random and systematic angular errors—was implemented and successfully tested on modeled data. To translate this potential into experimental observations a single-crystal goniometer setup was built and employed in extensive 11.8 T NMR observations. From these

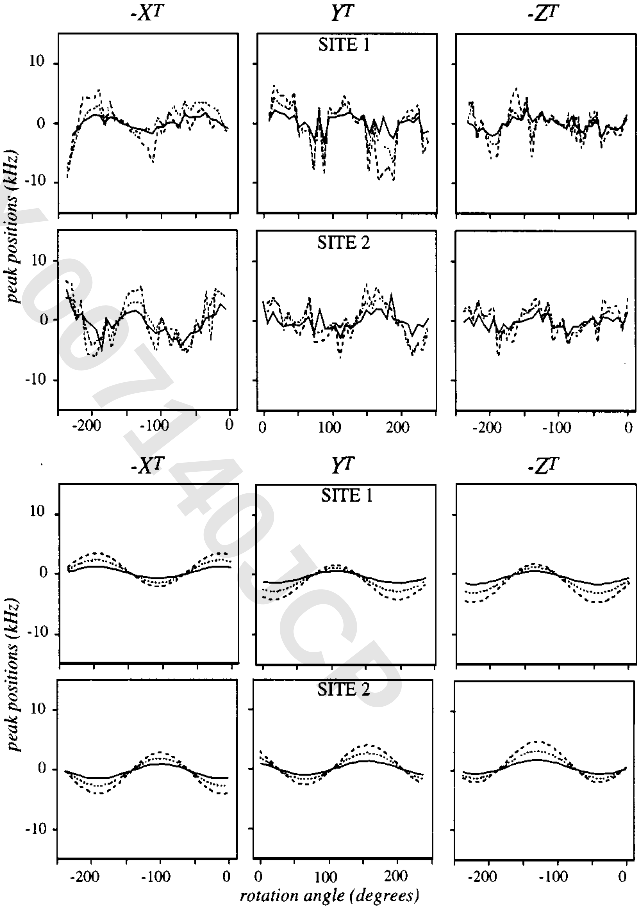

FIG. 9. Parameter plot residuals (top) and best ACS-quadrupole cross term fits (bottom) arising from the Co($acac$)$_3$ rotation data. For both experiments and fits plots assume the following frequency line combinations: $\upsilon_{3/2\leftrightarrow1/2}-\upsilon_{-1/2\leftrightarrow-3/2}$ (——); $\upsilon_{5/2\leftrightarrow3/2}-\upsilon_{-3/2\leftrightarrow-5/2}$ (-- - -); $\upsilon_{7/2\leftrightarrow5/2}-\upsilon_{-5/2\leftrightarrow-7/2}$ (— — —). Fitting of the experimental data resulted in $\delta^a_{ZX}=1000\pm500$ ppm, $\delta^a_{ZY}=-1000\pm500$ ppm, $\delta^a_{XY}=1000\pm1000$ ppm.

measurements reliable quadrupolar and CSA parameters could be extracted, together with the experimental plots in Fig. 9 reflecting the influence of the antisymmetric components of the shielding tensor.

Although these rotations provide quadrupolar-ACS cross-correlation data that constitute a valid starting point toward direct ACS determinations, it is also true that it is hard to discern in them an unambiguous message regarding the ACS elements' values. We believe that to a large extent this is a result of the actual compound which was used in the analysis: the ^{59}Co site in Co$(acac)_3$ possesses a relatively symmetric metal center devoid of substantial quadrupolar or shielding anisotropies, and thus is probably not the most suitable choice for such study. Unfortunately, however, none of the several other compounds that were assayed for this study grew crystals of sufficiently high quality to enable careful observations on all the satellite transitions over a complete rotation range. Efforts to remedy such deficiencies are still underway. A second technical challenge found during the course of these measurements arose from the presence of potential angular errors in the rotation plots. Particularly hard to achieve was an exact orthogonal alignment of the axis of rotation with respect to the magnetic field. This problem is usually solved in MAS NMR spectroscopically by maximizing the number of observable rotational echoes, and can lead in favorable cases to an angle setting accuracy better than 0.01°. The lack of a similar protocol in the present static case yielded degrees of alignments that were poorer than this figure by an order of magnitude; we are currently exploring further improvements in the single-crystal rotation procedures relying on mechanical or optical alignment techniques.

From a spectroscopic standpoint, it is also interesting to note that quadrupole effects will introduce nonsecular terms arising from the conventional chemical shielding anisotropy. Formally this phenomenon is related to the quadrupole-driven reintroduction of dipolar couplings to spin-1/2 nuclei recently discussed by Wu and Wasylishen,[39] which was also shown to affect solely the quadrupole's satellite transitions. As mentioned such effects have been recently noted on $I=1$ systems, and according to the simulations in Fig. 1 they should also become directly observable for half-integer quadrupolar nuclei via 2D correlations between satellite and central transitions under MAS condition. Additional efforts to detect such phenomena are also underway.

ACKNOWLEDGMENTS

We are grateful to Professor G. Harbison (Univ. Nebraska—Lincoln) for valuable discussions and to Jose Ortiz (Univ. Illinois—Chicago) for assistance in the processing and measurement of data. This work was supported by the U.S. National Science Foundation through grants DMR-9806810 and CHE-9841790 (Creativity Extension Award), by the U. S. Department of Energy through Grant 00ER15049, as well as by a Philip M. Klutznick Fund for Research (Weizmann Institute). L.F. is a Camille Dreyfus Teacher-Scholar (1996-2001).

APPENDIX

A summary of the expressions involved in the various $\{A_m^{(\lambda)}-E_m^{(\lambda)}\}_{\lambda=Q,\mathrm{CS}}$ coefficients appearing in Eqs. (30), (32) may be retrieved electronically from AIP's EPAPAS homepage (see Ref. 40).

[1] U. Haeberlen, in *Advances in Mangetic Resonance*, edited by J. S. Waugh (Academic, New York, 1976).
[2] H. W. Spiess, in *NMR Basic Principles and Progress*, edited by P. Diehl, E. Fluck, and R. Kosfeld (Springer-Verlag, New York (1978), Vol. 15.
[3] M. Mehring, *High Resolution NMR in Solids* (Springer-Verlag, Berlin, 1983).
[4] L. Frydman, Annu. Rev. Phys. Chem. **52**, 463 (2001).
[5] A. D. Buckingham and S. Malm, Mol. Phys. **22**, 1127 (1971).
[6] A. E. Hansen and T. D. Bouman, J. Chem. Phys. **91**, 3552 (1989).
[7] J. Kowalewski and L. Werbelow, J. Magn. Reson. **128**, 144 (1997).
[8] M. H. Cohen and F. Reif, Solid State Phys. **5**, 321 (1957).
[9] A. Abragam, *The Principles of Nuclear Magnetism* (Oxford University Press, Oxford, 1985).
[10] P. P. Man, in *Encyclopedia of NMR*, edited by D. M. Grant and R. K. Harris (Wiley, New York, 1995), p. 3838.
[11] D. L. VanderHart, H. S. Gutowsky, and T. C. Farrar, J. Am. Chem. Soc. **89**, 5056 (1967).
[12] A. Naito, S. Ganapathy, and C. A. McDowell, J. Chem. Phys. **74**, 5393 (1981).
[13] J. G. Hexem, M. H. Frey, and S. J. Opella, J. Chem. Phys. **77**, 3847 (1982).
[14] A. C. Olivieri, L. Frydman, and L. E. Diaz, J. Magn. Reson. (1969-1992) **75**, 50 (1987).
[15] R. K. Harris and A. C. Olivieri, Prog. Nucl. Magn. Reson. Spectrosc. **24**, 435 (1992).
[16] M. Bloom and M. A. LeGros, Can. J. Phys. **64**, 1522 (1986).
[17] R. Tycko and S. J. Opella, J. Am. Chem. Soc. **108**, 3531 (1986).
[18] R. Tycko, P. L. Stewart, and S. J. Opella, J. Am. Chem. Soc. **108**, 5419 (1986).
[19] R. Tycko and S. J. Opella, J. Chem. Phys. **86**, 1761 (1987).
[20] L. Marinelli, S. Wi, and L. Frydman, J. Chem. Phys. **110**, 3100 (1999).
[21] H. J. Jakobsen, H. Bildsøe, J. Skibsted, and T. Giavani, J. Am. Chem. Soc. (in press).
[22] W. S. Veeman, Philos. Trans. R. Soc. London, Ser. A **299**, 629 (1981).
[23] U. Haeberlen and J. S. Waugh, Phys. Rev. **175**, 453 (1968).
[24] S. Wi and L. Frydman, J. Chem. Phys. **112**, 3248 (2000).
[25] J. Mason, Chem. Rev. **87**, 1299 (1987).
[26] J. Mason, Ed. *Multinuclear NMR* (Plenum, New York, 1987).
[27] A. Medek, J. S. Harwood, and L. Frydman, J. Am. Chem. Soc. **117**, 12779 (1995).
[28] Z. H. Gan, J. Am. Chem. Soc. **122**, 3242 (2000).
[29] H. W. Spiess, H. Haas, and H. Hartmann, J. Chem. Phys. **50**, 3057 (1969).
[30] H. W. Spiess and R. K. Shelline, J. Chem. Phys. **53**, 3036 (1970).
[31] E. C. Reynhardt, Can. J. Phys. **52**, 1398 (1974).
[32] S. Hayashi, Magn. Reson. Chem. **34**, 791 (1996).
[33] K. Eichele, J. C. C. Chan, R. E. Wasylishen, and J. F. Britten, J. Phys. Chem. A **101**, 5423 (1997).
[34] G. J. Kruger and E. C. Reynhardt, Acta Crystallogr., Sect. B: Struct. Crystallogr. Cryst. Chem. **30**, 822 (1974).
[35] T. Vosegaard, V. Langer, P. Daugaard, E. Hald, H. Bildsøe, and H. J. Jakobsen, Rev. Sci. Instrum. **67**, 2130 (1996).
[36] T. Vosegaard, J. Skibsted, H. Bildsøe, and H. J. Jakobsen, J. Magn. Reson., Ser. A **122**, 111 (1996).
[37] T. Vosegaard, I. P. Byriel, L. Binet, D. Massiot, and H. J. Jakobsen, J. Am. Chem. Soc. **120**, 8184 (1998).
[38] P. H. William, P. F. Brian, A. T. Saul, and T. V. William, *Numerical Recipes* (Cambridge University Press, Cambridge, 1992).
[39] G. Wu and R. E. Wasylishen, Mol. Phys. **95**, 1177 (1998).
[40] See EPAPS Document No. E-JCPSA6-115-007140 for a description of the coefficients involved in Eqs. (30) and (32). This document may be retrieved via the EPAPS homepage (http://www.aip.org/pubservs/epaps.html) or from ftp.aip.org in the directory /epaps/. See the EPAPS homepage for more information.